



Cite this: *RSC Adv.*, 2022, 12, 21026

# Efficient degradation of organic dyes using peroxymonosulfate activated by magnetic graphene oxide†

Yawei Shi,  Haonan Wang, Guobin Song, Yi Zhang, Liya Tong, Ya Sun and Guanghui Ding\*

Magnetic graphene oxide (MGO) was prepared and used as a catalyst to activate peroxymonosulfate (PMS) for degradation of Coomassie brilliant blue G250 (CBB). The effects of operation conditions including MGO dosage, PMS dosage and initial concentration of CBB were studied. CBB removal could reach 99.5% under optimum conditions, and high removals of 98.4–99.9% were also achieved for other organic dyes with varied structures, verifying the high efficiency and wide applicability of the MGO/PMS catalytic system. The effects of environmental factors including solution pH, inorganic ions and water matrices were also investigated. Reusability test showed that CBB removals maintained above 90% in five consecutive runs, indicating the acceptable recyclability of MGO. Based on quenching experiments, solvent exchange ( $\text{H}_2\text{O}$  to  $\text{D}_2\text{O}$ ) and *in situ* open circuit potential (OCP) test, it was found that  $\cdot\text{OH}$ ,  $\text{SO}_4^{\cdot-}$  and high-valent iron species were responsible for the efficient degradation of CBB in the MGO/PMS system, while the contributions of  $\text{O}_2^{\cdot-}$ ,  $^1\text{O}_2$  and the non-radical electron-transfer pathway were limited. Furthermore, the plausible degradation pathway of CBB was proposed based on density functional theory (DFT) calculations and liquid chromatography-mass spectrometry (LC-MS) results, and toxicity variation in the degradation process was evaluated by computerized structure–activity relationships (SARs) using green algae, daphnia, and fish as indicator species.

Received 7th June 2022

Accepted 5th July 2022

DOI: 10.1039/d2ra03511a

rsc.li/rsc-advances

## 1. Introduction

Various organic pollutants in water including dyes, antibiotics and phenolic compounds pose potential threats to aquatic organisms and human health. Compared to physical treatment technologies such as adsorption, coagulation and membrane separation, the advanced oxidation process (AOP) is considered as an attractive approach due to its wide applicability and its ability to achieve degradation or even mineralization of contaminants. Recently, persulfates including peroxymonosulfate (PMS) and peroxydisulfate (PDS) have been widely employed as green oxidants in AOP.<sup>1,2</sup> Persulfates are easy to transport and store due to their solid nature at ambient conditions. After use, they are converted into nontoxic sulfate anions, the release of which is considered acceptable through optimization of the oxidant dosage and further application of treated water.<sup>3</sup>

Although persulfates can directly react with some pollutants by non-radical oxidation, the relatively low reaction rate and mineralization degree hindered the application of this

approach.<sup>4,5</sup> Therefore, activation of persulfates is generally required. Compared to PDS possessing a stable symmetric structure, the activation of asymmetric PMS is easier and stronger oxidation performance to mineralize pollutants is expected. The input of external energy, such as heat,<sup>6</sup> light,<sup>7</sup> ultrasound<sup>8</sup> and electricity<sup>9</sup> can trigger the activation of PMS to produce reactive oxygen species (ROSs) such as sulfate radicals ( $\text{SO}_4^{\cdot-}$ ), hydroxyl radicals ( $\cdot\text{OH}$ ) and singlet oxygen ( $^1\text{O}_2$ ), which possess strong oxidative ability and promote the degradation of organic pollutants. Besides, catalysts are also extensively employed for PMS activation. Although transition metal ions ( $\text{Co}^{2+}$ ,  $\text{Fe}^{2+}$ ,  $\text{Cu}^+$ , *etc.*) can highly efficiently activate PMS, the residue metal ions in treated water may be a potential concern and need further treatment. Considering this, metal-based heterogeneous catalysts are receiving increasing attention, and iron-based heterogeneous catalysts stand out due to the lower cost and lower toxicity of Fe compared other transition metals.<sup>10</sup> Among various iron-based catalysts,  $\text{Fe}_3\text{O}_4$  which can be facilely separated from water after use by an external magnetic field may be a feasible choice.<sup>11</sup> However,  $\text{Fe}_3\text{O}_4$  nanoparticles are easy to aggregate and their catalytic activities are thus diminished.<sup>12</sup> To solve this problem, dispersion of  $\text{Fe}_3\text{O}_4$  nanoparticles onto certain supports can help to enhance the catalytic activity through synergetic effects between  $\text{Fe}_3\text{O}_4$  and the support.<sup>13–15</sup>

College of Environmental Science and Engineering, Dalian Maritime University, Dalian 116026, China. E-mail: guanghuiding@dlmu.edu.cn

† Electronic supplementary information (ESI) available. See <https://doi.org/10.1039/d2ra03511a>



On the other hand, carbon materials with large surface areas and rich functionalities are also widely investigated for persulfate activation. Graphene oxide (GO) is a well-known carbon material with a two-dimensional structure and abundant oxygen-containing functional groups, which has attracted global attention since its birth.<sup>16</sup> GO and its derivatives have been successfully applied for persulfate activation towards efficient degradation of organic pollutants in water.<sup>17–20</sup> Nevertheless, due to the well dispersion of GO in water, the separation of GO after the catalytic process is difficult, and the residual GO in water may pose some negative impacts on the ecological system.<sup>21</sup> Considering this, GO can be combined with Fe<sub>3</sub>O<sub>4</sub> to prepare Fe<sub>3</sub>O<sub>4</sub>-GO composite materials known as magnetic GO (MGO), which are endowed with large surface area, rich functionalities as well as magnetic property and can be considered as promising candidates for water treatment.

In our recent work,<sup>22</sup> MGO has been prepared in a facile co-precipitation method and then utilized for methylene blue adsorption, where the PMS oxidation method has been found to be a favorable approach for regeneration of spent MGO. In this work, we further used MGO as a catalyst to activate PMS for degradation of Coomassie brilliant blue G250 (CBB). Although magnetic graphene-based materials have been used for the catalytic degradation of various organic pollutants,<sup>23–27</sup> graphene and reduced graphene oxide (rGO) rather than pristine graphene oxide are usually used in these reports. Graphene and rGO are generally prepared by reduction of GO, thus the utilization of GO can help to simplify the whole preparation procedure. Besides, the different properties between GO and graphene/rGO may influence the reaction mechanism, which needs further evaluation. In addition, to the best of our knowledge, the degradation of CBB is seldom investigated in persulfate-based systems. CBB belongs to the triphenylmethane dyes, which contain three phenyl groups linked by a central carbon atom and generally possess mutagenic and carcinogenic properties, posing major health risks to human.<sup>28</sup> Besides its frequent utilization in textile industry, CBB is also widely used for quantifying proteins as well as other biological applications.<sup>29</sup> The CBB solution was found to be significantly toxic to wheat seeds, suppressing their germination and growth.<sup>30</sup> So far, the oxidative removal of CBB has been investigated in photocatalytic<sup>31,32</sup> and sonochemical<sup>33</sup> processes. Recently, an integrated process combining hydrodynamic cavitation, hydrogen peroxide and PDS has been employed for the degradation of CBB, where the activation of PDS was achieved due to the thermal effect of the hydrodynamic cavitation process.<sup>34</sup> Thus, further research is needed to explore the performances of persulfate-based catalytic systems for CBB degradation. In the current work, the effects of operation conditions and environmental factors on CBB degradation were investigated. The impacts of these factors were also evaluated in the previous work.<sup>22</sup> However, as a different treatment approach and a different target dye were used in the current work, the results and corresponding mechanisms should be further addressed. Moreover, since the previous work was mainly focused on adsorption treatment of MB, the degradation pathway upon PMS oxidation was not investigated. Considering the larger

molecular weight and more complex structure of CBB compared to MB, density functional theory (DFT) calculations have been used to help to propose its degradation pathway. We also used computerized structure activity relationships (SARs) to evaluate the toxicity variation considering the emergence of various products in the degradation process of CBB.

## 2. Experimental

### 2.1. Materials and characterizations

The MGO catalyst was prepared in a co-precipitation method as described in our previous work.<sup>22</sup> In brief, (NH<sub>4</sub>)<sub>2</sub>Fe(SO<sub>4</sub>)<sub>2</sub>·6H<sub>2</sub>O, NH<sub>4</sub>Fe(SO<sub>4</sub>)<sub>2</sub>·12H<sub>2</sub>O and GO were mixed in water and heated at 85 °C. Aqueous ammonia was added subsequently under nitrogen protection, and the mixture was stirred for 1 h and cooled naturally. Finally, the precipitate was magnetically separated, rinsed, and dried to obtain MGO. The fresh and used MGO catalysts were characterized by nitrogen sorption (Autosorb-iQ-C, Quantachrome, US), X-ray photoelectron spectroscopy (XPS, ESCALAB 250Xi, Thermo Fisher, US) and X-ray diffraction (XRD, D8 ADVANCE, Bruker, Germany) measurements. The leached concentration of iron in the treated water was tested by inductively coupled plasma-mass spectrometry (ICP-MS, Agilent 7800, US). The total organic carbon (TOC) content was measured with a TOC analyzer (Multi N/C 2100, Analytik Jena, Germany). The open circuit potential (OCP) test was conducted with a CHI660E electrochemical workstation (Chenhua, China). The treated water sample was analyzed with an ultra-high performance liquid chromatography (UPLC) system (Agilent 1290, US) coupled to a mass spectrometer (QTOF6550, US) with an electron spray ionization (ESI) source in the positive ion mode. More details for the materials and characterization methods were provided in Text S1.1 in ESI Materials.†

### 2.2. Catalytic oxidation experiments

The catalytic oxidation of CBB was conducted in a glass flask under mechanical stirring (500 rpm) by adding MGO and PMS to a dye solution. The initial concentration of the dye solution was in the range of 25–100 mg L<sup>−1</sup>, which was selected based on previous reports.<sup>32–35</sup> The initial pH was tailored when needed with aqueous NaOH after the addition of PMS. NaCl, NaHCO<sub>3</sub> or Na<sub>2</sub>HPO<sub>4</sub> was added when needed. These ions commonly found in real water matrices may influence the efficiency of the catalytic oxidation process, and the addition of them could help to provide more data for potential practical applications. Quenchers including 2 M methanol (MA), 2 M *tert*-butanol (TBA), 1 mM furfuryl alcohol (FFA), 10 mM benzoquinone (BQ) and 0.2 mM methyl phenyl sulfoxide (PMSO) were added when needed. PMSO was added as a quencher for high-valent iron-oxo species<sup>36</sup> considering the presence of iron species in the catalyst. To investigate the effect of water matrix, tap water, lake water or sea water was spiked with CBB. To test the reusability of the catalyst, the spent MGO catalyst was magnetically separated and washed with 2 L g<sup>−1</sup> water for the next catalytic oxidation run. To investigate the solid concentration of CBB, spent MGO

was magnetically separated and then extracted with ethanol twice by sonication to obtain two liquid samples. To investigate the contribution of leached Fe ion, 0.5 g L<sup>-1</sup> MGO was first stirred with 2 mM aqueous PMS for 5 h and then magnetically removed. After that, 50 mg L<sup>-1</sup> CBB was added to the solution to start the catalytic oxidation reaction. In this way, the homogeneous iron species were introduced *in situ*, and the contribution of homogeneous reaction could be better evaluated. The catalytic oxidation experiments for methylene blue (MB), Rhodamine B (RhB), basic blue 17 (BB17) and methyl orange (MO) were performed as well. The concentrations of the dyes were analyzed with a UV-visible spectrometer (TU-1901, Beijing Puxi, China) at 584, 664, 554, 630 and 506 nm for CBB, MB, RhB, BB17 and MO respectively. Control tests without PMS addition were also conducted at a series of initial pH. The removal of dye was calculated by eqn (1):

$$\text{Removal (\%)} = 100(C_0 - C)/C_0 \quad (1)$$

where  $C_0$  is the initial concentration of dye and  $C$  is the concentration at time  $t$ .

The apparent rate constant ( $k_{\text{app}}$ ) in the catalytic oxidation process was obtained from pseudo-first-order kinetic model (eqn (2)) by linear regression:

$$\ln(C/C_0) = -k_{\text{app}}t \quad (2)$$

The oxidation or adsorption experiments were conducted at least in duplicates to report average results with error bars.

### 2.3. Theoretical calculation and toxicity evaluation

The structure of CBB was constructed and then optimized using the DFT/B3LYP method with the 6-31g(d,p) basis set considering the solvent effect by the Solvation Model based on Density (SMD) with Gaussian 16 program.<sup>37</sup> Frequency analysis was performed at the same level to confirm the structure. The orbital-weighted Fukui functions of  $f_{\text{OW}}^-$  and  $f_{\text{OW}}^0$  as well as condensed Fukui indexes were calculated using the wavefunction analysis program of Multiwfn<sup>38</sup> and the images were further optimized with the Virtual Molecular Dynamic (VMD) software.<sup>39</sup> Compared to the methods based on the Frontier Molecular Orbital (FMO) theory, the orbital-weight Fukui function put different weight to all molecular orbitals and is considered to perform better for reactivity prediction.<sup>40,41</sup> The acute and chronic toxicities of the parent CBB and its oxidation products to aquatic organisms of three trophic levels (green algae, daphnia, and fish) were evaluated with the Ecological Structure Activity Relationships (ECOSAR) V2.0 program using computerized SARs.

## 3. Results and discussion

### 3.1. Characterizations of the catalyst

The MGO composite material employed in this work was prepared in the same manner as described in our previous work,<sup>22</sup> where characterization results of transmission electron microscopy (TEM), XRD, Fourier transform infrared (FTIR),

XPS, vibrating sample magnetometry (VSM), nitrogen sorption and zeta potential measurements were comprehensively reported. In brief, TEM, XRD, FTIR, and XPS results showed that the material was composed of Fe<sub>3</sub>O<sub>4</sub> and GO with abundant -OH and -C=O groups. VSM test proved the magnetic separation property of MGO, showing a saturation magnetization of 23.0 emu g<sup>-1</sup>. Nitrogen sorption test verified the porous nature of MGO with a specific surface area ( $S_{\text{BET}}$ ) of 173 m<sup>2</sup> g<sup>-1</sup> and a pore volume of 0.299 cm<sup>3</sup> g<sup>-1</sup>, and the isoelectric point (IEP) of MGO was estimated to be 5.2 according to zeta-potential measurements.

### 3.2. Catalytic performance

To investigate the catalytic performance of MGO for CBB oxidation, the effects of operation conditions including MGO dosage, PMS dosage and initial concentration of CBB were studied. As illustrated in Fig. 1a, the removal of CBB was 41% with 2 mM PMS in the absence of MGO, which was attributed to the direct oxidation of CBB with PMS. However, limited TOC removals were generally observed in non-activated systems and activation of PMS towards deeper oxidation is essential from an environmental viewpoint.<sup>4,5</sup> When 0.3 g L<sup>-1</sup> MGO was added, the removal of CBB was drastically increased to 96.1%, indicating the efficient catalytic performance of MGO. Further increasing MGO dosage to 0.5 and 0.7 g L<sup>-1</sup> led to better CBB removals of 99.5% and >99.9% respectively (Fig. 1a) due to the presence of more active sites. The effect of PMS dosage was also studied (Fig. 1b). The removal of CBB was enhanced when PMS dosage was increased from 1 to 2 mM, but a further increase to 3 mM resulted in a slightly declined CBB removal. This was probably attributed to the self-quenching effect when excessive ROSs were produced, similar to the trend observed in previous works.<sup>25,42</sup> In addition, the concentration of TOC after the catalytic process was analyzed. The removal of TOC at 0.5 g L<sup>-1</sup> MGO and 2 mM PMS was found to be 50.9%, which was lower than the value of CBB removal (99.5%). This was ascribed to the incomplete oxidation of CBB in this process, indicating the formation of other oxidation intermediates. No improvement in TOC removal was observed by extending the reaction time to 480 min, which was probably ascribed to the exhaustion of PMS as an oxidant and the adsorption saturation on the catalyst surface. For comparison, the TOC removal in the absence of MGO was also measured and found to be only 6.2% (Fig. S1†). Both CBB and TOC removals obtained with the MGO/PMS system were much higher than those obtained with PMS only, which verified the superiority of the MGO catalyst.

When it came to the effect of initial CBB concentration, a higher concentration led to a lower removal (Fig. 1c). This was conceivable because of the relatively reduced amounts of PMS and catalytic sites at a higher CBB concentration. In addition, as discussed above, organic intermediates were formed during the oxidation process, and more intermediates could be produced when more pollutants were presented,<sup>43</sup> which exacerbated the shortage of oxidative species and catalytic sites. Despite of this fact, CBB removal could still reach a high value of 97.8% at initial CBB concentration of 100 mg L<sup>-1</sup>, indicating the efficient



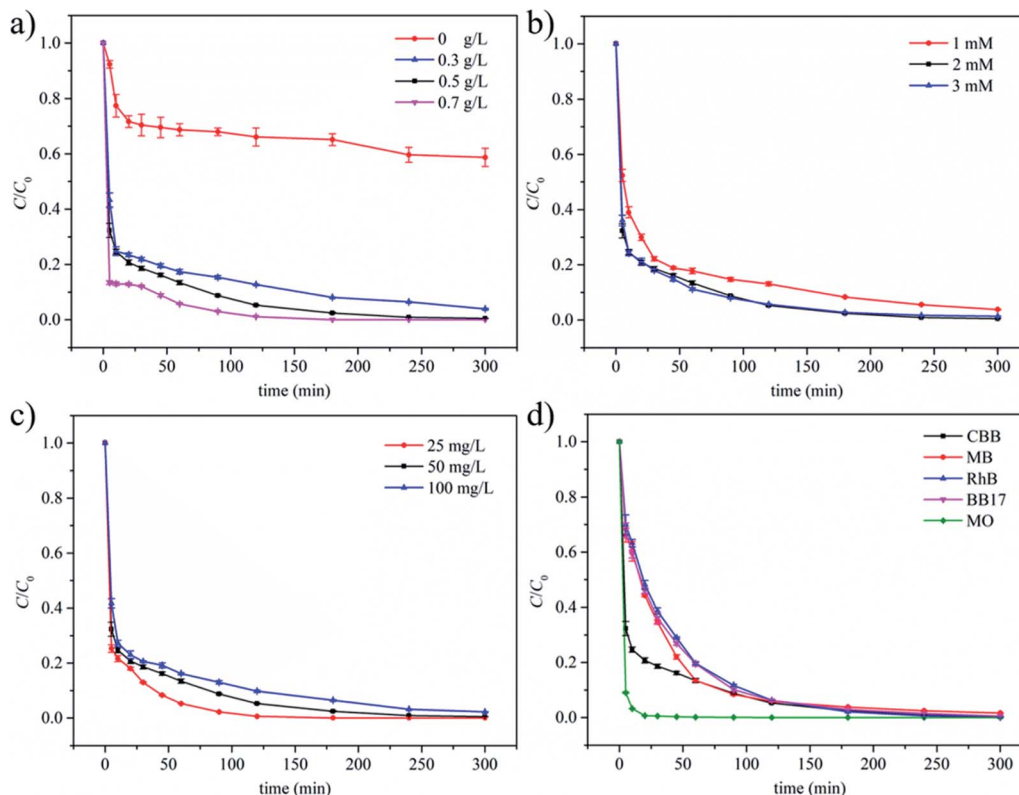


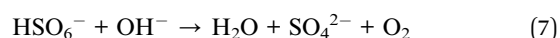
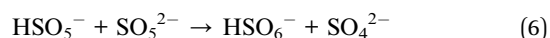
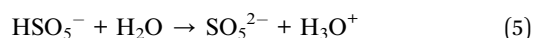
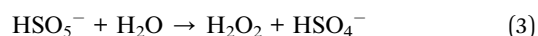
Fig. 1 Effect of MGO dosage (a), PMS dosage (b), initial concentration of CBB (c) on catalytic CBB oxidation and oxidation of various dyes (d). Experimental conditions: MGO dosage = 0.5 g L<sup>-1</sup>, PMS dosage = 2 mM, initial dye concentration = 50 mg L<sup>-1</sup>, temperature = 25 °C.

catalytic performance of the MGO/PMS system. Considering that CBB was an anionic dye, the oxidations of another typical anionic dye (MO) and three typical cationic dyes (MB, RhB and BB17) were conducted as well. High removals of 98.4–99.9% were achieved (Fig. 1d) for these dyes with varied structures, verifying the wide applicability of the MGO/PMS catalytic system.

### 3.3. Effect of pH

The above experiments were conducted in deionized (DI) water without pH tailoring. After the addition of MGO and PMS, the solution pH dropped to around 2.7 immediately and further dropped to 2.5 after the oxidation process, which was ascribed to the acid nature of PMS<sup>44</sup> and the possible formation of acidic oxidation intermediates. For real water treatment, the pH value may vary significantly and impact the performance of the MGO/PMS system. To address this issue, additional oxidation experiments were conducted by adjusting the solution pH to 5.0, 7.1, 9.0 and 11.0 after PMS was added. As depicted in Fig. 2a, high CBB removals similar to the case without pH adjustment were obtained at pH 5.0, 7.1 and 9.0. According to the local standard of GB 18918-2002 in China, the pH of wastewater was regulated to be in the range of 6–9. Thus, the result here indicated that the MGO/PMS system was applicable to most practical pH conditions. The slightly enhanced removal efficiency at pH 9.0 was attributed to the alkaline activation of PMS under a weak alkaline condition (eqn (3) and (4)), in line with the result

reported previously.<sup>45–47</sup> From a practical viewpoint, pre-adjustment of pH to 9.0 may be the optimum choice. Under this condition, the removal efficiency was enhanced, and the final pH value was close to neutral, making it possible to avoid the post-adjustment of pH before discharging the treated water. When the initial pH was tailored to 11.0, CBB removal dropped to 90.1% after being treated for 300 min (Fig. 2a). The declined removal under the strong alkaline condition was attributed to the decomposition of PMS without generating ROS triggered by excessive OH<sup>-</sup> (eqn (5)–(7)).<sup>47,48</sup>



On the other hand, considering the porous structure of MGO, change in adsorptive behavior of PMS and CBB may also make a contribution. As mentioned above, IEP of MGO was 5.2, suggesting that the surface of MGO should be positively charged at pH < 5.2 and negatively charged at pH > 5.2. For PMS, the fraction of SO<sub>5</sub><sup>2-</sup>, which was an divalent anion, would increase





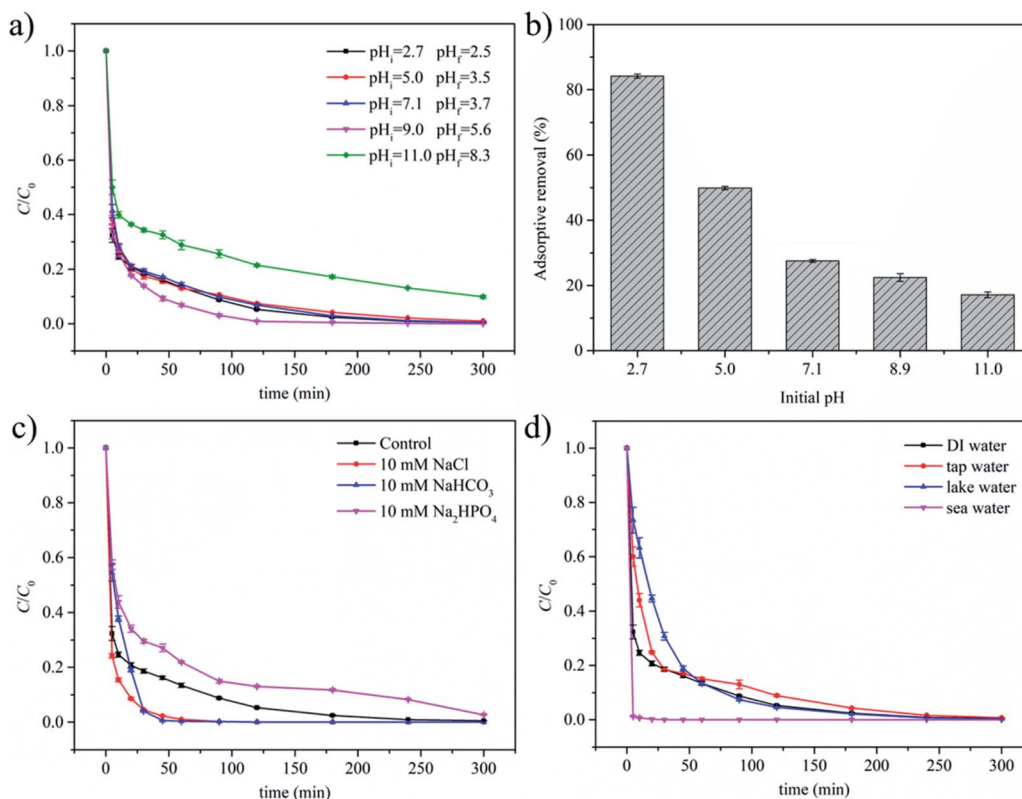


Fig. 2 Effect of pH on catalytic CBB oxidation (a), adsorptive removal of CBB with MGO only (b), effect of inorganic ions (c) and water matrix (d) on CBB oxidation. Experimental conditions: MGO dosage = 0.5 g L<sup>-1</sup>, PMS dosage = 2 mM, initial CBB concentration = 50 mg L<sup>-1</sup>, temperature = 25 °C.

sharply when the solution pH reached 9.4 (the  $pK_{a2}$  of PMS).<sup>49</sup> Thus, enhanced electrostatic repulsion between PMS and MGO surface at pH > 9.4 would weaken the adsorption and subsequent activation of PMS, leading to a decline in ROS generation and thus CBB degradation. For CBB, chromophores were included in its anionic organic part, so an increase in pH should be unfavorable for CBB adsorption due to enhanced electrostatic repulsion. The adsorptive removals of CBB at different initial pH values were shown in Fig. 2b. As expected, a continuous drop in adsorptive CBB removal was observed with increasing initial pH. According to previous reports,<sup>50,51</sup> the efficient adsorption of organic pollutants on the catalyst surface could facilitate their degradation in the persulfate activation process, leading to enhanced removal efficiency. At pH 11.0, the adsorption of CBB was suppressed most significantly. This reason, as well as the useless decomposition and suppressed adsorption of PMS discussed above, hindered the degradation of CBB collectively and led to the lowest removal of CBB. For the cases at initial pH values of 5.0, 7.1 and 9.0, high CBB removals could still be achieved despite of the suppressed CBB adsorption, indicating that adsorption was not the rate-determining step under these conditions.

The UV-visible spectra of parent CBB, CBB after adsorption and CBB after catalytic oxidation as well as the corresponding optical photos were shown in Fig. S2.† The absorbance at 584 nm for CBB after catalytic oxidation was lower than that for

CBB after adsorption (Fig. S2a†), in accordance with the lighter color and higher CBB removal in the former case (Fig. S2b†). By comparing the removals with and without PMS at pH 2.7 (the case without pH adjustment), it seemed that the contribution of catalytic oxidation was quite limited, which was calculated to be only 15.3% by subtracting the value without PMS (84.2%) from the value with PMS (99.5%). However, it should be noted that this was not the truth. To illustrate this point, the spent MGO samples after catalytic oxidation (with PMS) and adsorption (without PMS) were extracted with ethanol twice and the optical photos of the ethanol samples were displayed in Fig. S3.† The two samples obtained after catalytic oxidation were colorless, in contrast to the blue color of the samples obtained after adsorption. After being adsorbed by MGO in the catalytic oxidation system, the CBB molecules in the solid phase did not remain intact but were oxidized and transformed into colorless species. In other words, although adsorption played an indispensable role in the efficient catalytic oxidation process, the final “apparent” contribution attributed to adsorption was limited. This result clearly demonstrated the superiority of the MGO/PMS system, where low residue CBB concentrations were achieved in both the aqueous and solid phases. This one of the main advantages of the catalytic oxidation system compared to the adsorption one. Besides, extreme acidic conditions were required for the adsorption system, which limited its application in large scales. Finally, from the viewpoint of cost, both pre-



adjustment and post-adjustment of pH were needed for the adsorption system, while post-adjustment of pH may be avoided for the catalytic oxidation system at the optimum initial pH of 9.0. The use of PMS as an oxidant could bring additional cost. However, the spent MGO could be easily regenerated by washing with water in the catalytic oxidation system, while alkaline solutions or organic solvents were often required for the regeneration of used adsorbents in the adsorption system. Thus, a relatively lower cost is expected for the catalytic oxidation system. Considering all the above aspects, the catalytic oxidation system is better than the adsorption one.

### 3.4. Effect of inorganic ions and water matrix

Background inorganic ions present in real waters may also influence the efficiency of the catalytic oxidation process. The effects of  $\text{Cl}^-$ ,  $\text{HCO}_3^-$  and  $\text{HPO}_4^{2-}$  as typical inorganic ions were investigated. As illustrated in Fig. 2c, the removal of CBB was accelerated upon the addition of 10 mM  $\text{Cl}^-$ . The reactions between  $\text{Cl}^-$  and ROS such as  $\text{SO}_4^{\cdot-}$  and  $^{\cdot}\text{OH}$  could lead to the production of chlorine radicals such as  $\text{Cl}_2^{\cdot-}$ . According to a previous report, although the redox potential of  $\text{Cl}_2^{\cdot-}$  was relatively lower than  $\text{SO}_4^{\cdot-}$  and  $^{\cdot}\text{OH}$ , it may be produced in larger amounts, offsetting the scavenging effects of  $\text{SO}_4^{\cdot-}$  and  $^{\cdot}\text{OH}$ .<sup>52,53</sup> In addition,  $\text{Cl}^-$  was reported to react with PMS directly, forming active species such as  $\text{HOCl}$  to participate in the oxidation of organic pollutants.<sup>54</sup> This point was verified by the oxidation experiments of CBB with the PMS/ $\text{Cl}^-$  system at different  $\text{Cl}^-$  concentrations without MGO. As illustrated in Fig. S4a,† almost complete removals of CBB were achieved at 10–2000 mM  $\text{Cl}^-$ , verifying that the presence of  $\text{Cl}^-$  was conducive to the oxidation of CBB.

Upon the addition of 10 mM  $\text{HCO}_3^-$ , the initial pH was around 8.6 and remained stable during the whole process due to the buffering effect of  $\text{HCO}_3^-$ . This was different from the situation when the initial pH was adjusted to 9.0 by NaOH, where the solution pH dropped gradually and finally reached 5.6. Since the weak alkaline condition remained stable in the presence of 10 mM  $\text{HCO}_3^-$ , the adsorption of CBB should be suppressed in a larger degree. In addition,  $\text{HCO}_3^-$  could act as a quencher and react with  $\text{SO}_4^{\cdot-}$  and  $^{\cdot}\text{OH}$ , generating less active species such as  $\text{HCO}_3^{\cdot}$  and  $\text{CO}_3^{\cdot-}$ .<sup>55</sup> However, the stable weak alkaline condition could also favor the decomposition of PMS, fascinating the formation of ROS.<sup>54</sup> That is to say, the presence of  $\text{HCO}_3^-$  could exert multiple impacts on the degradation process. As shown in Fig. 2c, when 10 mM  $\text{HCO}_3^-$  was added, the removal of CBB lagged that of control in the first 20 min and then became faster, reaching a final value of 99.9% at 300 min. It was inferred that the suppression effects played a determining role in the early stage of the process. After that, the suppression effects became less important due to the gradual consumption of  $\text{HCO}_3^-$ , and the promotion of PMS decomposition seized the dominant position. The dual functions of  $\text{HCO}_3^-$  were also reflected from the CBB removals in the PMS/ $\text{HCO}_3^-$  system at different  $\text{HCO}_3^-$  concentrations without MGO (Fig. S4b†). The removal of CBB was 48.3% with 10 mM  $\text{HCO}_3^-$  and 2 mM PMS, higher than the value of 41.3% with PMS only,

indicating that a suitable amount of  $\text{HCO}_3^-$  was beneficial. A further increase to 100 mM  $\text{HCO}_3^-$  boosted CBB removal to 98.5%, but higher  $\text{HCO}_3^-$  dosages resulted in dramatically declined values even lower than 41.3%, verifying that excessive  $\text{HCO}_3^-$  became detrimental to CBB oxidation. According to previous reports<sup>56–58</sup> and the discussions above, the effects of  $\text{HPO}_4^{2-}$  on CBB oxidation should also be multiple, including (1) favoring the decomposition of PMS and accelerating the generation of ROS, (2) creating a weak alkaline environment and suppressing CBB adsorption to MGO, (3) combining with the iron-containing active sites on surface of MGO. As illustrated in Fig. 2c, the addition of 10 mM  $\text{HPO}_4^{2-}$  hindered the removal of CBB to some extent, and a relatively lower removal of 97.4% was obtained. This result suggested that the latter two negative impacts were dominant in the MGO/PMS system. In contrast, in the absence of MGO, CBB removal was enhanced with the addition of  $\text{HPO}_4^{2-}$  due to its beneficial effect (Fig. S4c†).

To further study the effects of water matrices, real water including tap water, lake water and sea water were spiked with CBB and then treated with the MGO/PMS system. The properties of different water matrices employed here were provided in Table S1.† The removal efficiencies in tap water and lake water were slightly lower than that in DI water (Fig. 2d), which was mainly attributed to the presence of varied inorganic ions and natural organic matters in them.<sup>59</sup> Despite of this, high removals close to that in DI water could be obtained, indicating the wide applicability of the MGO/PMS system for different water matrices. For sea water, the removal of CBB was very fast, reaching 99.8% after a short reaction time of 20 min. This was ascribed to the high concentration of  $\text{Cl}^-$  ions in sea water which greatly promoted the oxidation process.

### 3.5. Reusability test

From a practical viewpoint, reusability of the catalyst is an important issue. After the first catalytic oxidation run, the spent MGO catalyst was characterized by nitrogen sorption, XPS and XRD for comparison with the fresh one (Fig. 3a–c). The textural properties obtained from nitrogen sorption results and elemental compositions determined by XPS for fresh and spent catalysts were displayed in Table 1. Compared to the fresh catalyst, the spent one possessed reduced surface area, pore volume and average pore size. As discussed above, the amount of CBB was limited on the surface of spent MGO. Thus, the reduced porosity of spent MGO was attributed to the accumulation of oxidation intermediates on its surface. XPS results revealed a higher carbon content and the appearance of nitrogen and sulfur elements in spent MGO, which also suggested the presence of organic substance on its surface. In addition, the atomic ratio of nitrogen to sulfur in spent MGO was calculated to be 2.3, which deviated from the theoretical value of 1.5 calculated from the molecular formula of CBB ( $\text{C}_{47}\text{H}_{48}\text{N}_3\text{NaO}_7\text{S}_2$ ). This also suggested that it was oxidation intermediates rather than the parent CBB that was presented on the surface of spent MGO. High resolution analysis of C 1s, O 1s and Fe 2p spectra for both samples was further performed. As

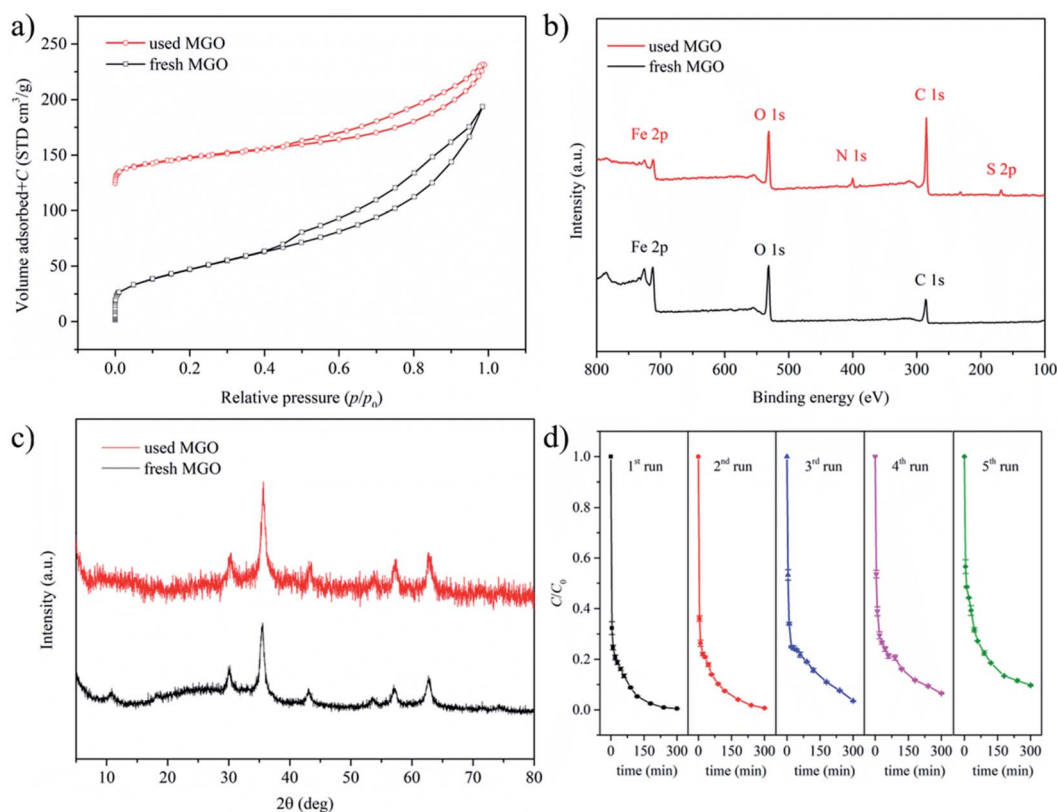


Fig. 3 Nitrogen sorption isotherms (a), XPS spectra (b) and XRD patterns (c) of fresh and used MGO; reusability of MGO for catalytic CBB oxidation (d). Experimental conditions: MGO dosage = 0.5 g L<sup>-1</sup>, PMS dosage = 2 mM, initial CBB concentration = 50 mg L<sup>-1</sup>, temperature = 25 °C.

Table 1 Textural properties and elemental compositions of fresh and used MGO

Sample	Textural properties			Elemental compositions (atom%)				
	$S_{\text{BET}}$ (m <sup>2</sup> g <sup>-1</sup> )	$V_{\text{total}}$ (cm <sup>3</sup> g <sup>-1</sup> )	$D_p$ (nm)	C	O	Fe	N	S
Fresh	173	0.299	6.91	44.7	37.9	17.4	—	—
Used	102	0.172	6.75	64.2	23.9	4.7	5.0	2.2

shown in Fig. S5a and b,† the three peaks in the C 1s spectra at round 284.8, 286.6 and 288.7 eV were ascribed to C–C/C=C, C–O, and C=O species respectively.<sup>12,24</sup> The fraction of C–C/C=C in used MGO was higher than that in the fresh one (Table S2†), again indicating the presence of organic substances on the surface of the used catalyst. Deconvolution of the O 1s spectra led to three peaks at 529.9, 531.2 and 532.5 eV (Fig. S5c and d†), which could be attributed to Fe–O, Fe–O–C and C–O species.<sup>12,24</sup> The decreased relative content of Fe–O in used MGO (Table S2†) could be attributed to the leaching of iron as well as the accumulation of organic substances on the catalyst surface. For the Fe 2p spectra, peaks for both Fe(II) and Fe(III) were observed (Fig. S5e and f†), and the relative contents of them did not changed significantly (Table S2†). This is in consistent with the XRD results (Fig. 3c), where the patterns of the two samples were similar to each other. In both patterns, the six diffraction peaks in the range of 30–65° could be attributed to Fe<sub>3</sub>O<sub>4</sub> (JCPDS 19-0629).

The spent MGO was washed with water and then used for the next catalytic oxidation run. As shown in Fig. 3d, CBB removals of five consecutive runs were 99.5%, 99.3%, 96.4%, 93.5% and 90.3% respectively. The decline in removal efficiency indicated that the oxidation intermediates on the catalyst surface could not be completely removed by washing. These intermediates occupied some active sites and consumed some oxidative species, leading to decreased CBB removals. Iron leaching could also play a role in the decreased activity, but its contribution was inferred to be limited considering the relatively low leaching amount and limited role of homogenous reaction in the MGO/PMS system.

### 3.6. Reaction mechanism

•OH and SO<sub>4</sub>•<sup>-</sup> as typical ROS are generally involved in PMS-based catalytic oxidation system. Thus, MA and TBA as widely used quenchers were first employed to investigate their



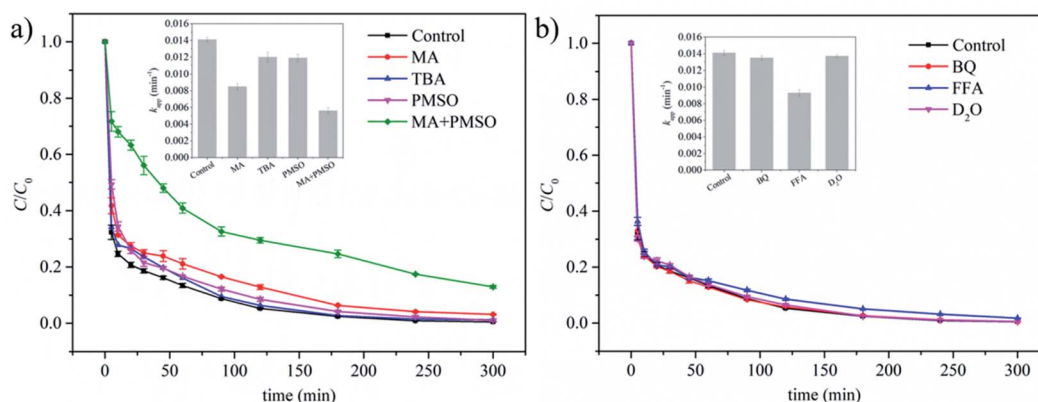


Fig. 4 Effects of MA, TBA, PMSO, MA + PMSO (a) and BQ, FFA,  $D_2O$  (b) on catalytic CBB oxidation. Insets are the corresponding apparent rate constants. Experimental conditions: MGO dosage =  $0.5 \text{ g L}^{-1}$ , PMS dosage =  $2 \text{ mM}$ , initial CBB concentration =  $50 \text{ mg L}^{-1}$ , temperature =  $25^\circ\text{C}$ .

contributions. MA is known as an effective quencher which could quickly quench both  $\cdot\text{OH}$  and  $\text{SO}_4^{\cdot-}$ ,<sup>60</sup> while TBA showed 1000 times higher reactivity towards  $\cdot\text{OH}$  than  $\text{SO}_4^{\cdot-}$ .<sup>24</sup> As shown in Fig. 4a, the addition of MA or TBA suppressed CBB removal, and the effect of MA was more significant. To further investigate their effects, the kinetic data were fitted in the pseudo-first-order model to obtain the apparent rate constant ( $k_{app}$ ) (Fig. S6a†). As compared in Fig. 4a inset,  $k_{app}$  decreased by 39.7% and 14.9% with the addition of MA and TBA respectively, suggesting that both  $\cdot\text{OH}$  and  $\text{SO}_4^{\cdot-}$  were involved in the oxidation process. However, the high final removal (96.8%) in the presence of MA suggested the existence of other reactive species. Recently, it was demonstrated that high-valent iron-oxo species played a role in the PMS-based oxidation process when iron-containing materials were used as the catalysts.<sup>36,61,62</sup> Similar to the case reported previously,<sup>36</sup>  $k_{app}$  for CBB removal decreased in the presence of PMSO (Fig. 4a). PMSO is known as a quencher for high-valent iron-oxo species.<sup>36</sup> Thus, this result indicated the involvement of high-valent iron-oxo species in the catalytic oxidation system. Similar to the cases with other quenchers, these reactive species were consumed by PMSO, leading to the decreased removal efficiency of CBB. Furthermore, when MA and PMSO were added simultaneously, a stronger inhibition effect was observed with 60.3% reduction in  $k_{app}$ . Under this circumstance, the final CBB removal was still relatively high, reaching 87.1%. One may argue that homogeneous reaction catalyzed by leached ions could also make a contribution. Leaching of iron was measured by ICP-MS and found to be  $3.74 \text{ mg L}^{-1}$  at initial pH of 2.7. The content of iron was calculated to be 47.1 wt% from XPS results (Table 1). Thus, the leaching ratio at  $0.5 \text{ g L}^{-1}$  MGO dosage was estimated to be 1.6%. The performances of Fe(II) and Fe(III) for homogeneous activation of PMS were significantly different.<sup>63</sup> The ICP result showed the total amount of leached iron but the ratio of Fe(II) and Fe(III) remained unknown. Thus, when conducting the experiment of leached iron, iron ions were introduced *in situ* as detailed in Section 2.2 rather than added directly. As illustrated in Fig. S6b,† the removal of CBB was promoted to some extent in the presence of *in situ* introduced leached ions compared to the

case of PMS only, but it was still far from the value obtained in the MGO/PMS system. Although leached ions made a contribution, the reaction mechanism in homogeneous systems were also generally related to  $\cdot\text{OH}$ ,  $\text{SO}_4^{\cdot-}$  and high-valent iron species.<sup>64</sup> Thus, in the MGO/PMS/MA + PMSO system, the contribution of leached ions could be ruled out because these species had been quenched. In addition, the metal species are less stable under acid conditions and the leaching amount generally decreases with increasing pH values.<sup>65–67</sup> As discussed in Section 3.3, high CBB removals similar to the case at pH 2.7 were obtained at pH 5.0, 7.1 and 9.0 and the pH of 9.0 may be the optimum choice. Thus, the leaching of iron at pH 9.0 was further investigated and found to be  $0.27 \text{ mg L}^{-1}$ , much lower than that obtained at pH 2.7. This was in accordance with previous reports and verified the increased stability of iron species with increasing pH.

Other reactive species such as superoxide radical ( $\text{O}_2^{\cdot-}$ ) and singlet oxygen ( $^1\text{O}_2$ ) may also play a part. BQ is considered as a quencher for  $\text{O}_2^{\cdot-}$ .<sup>68</sup> As shown in Fig. 4b, CBB removal was almost not influenced by the addition of BQ, which excluded the involvement of  $\text{O}_2^{\cdot-}$ . FFA is regarded as a quencher for  $^1\text{O}_2$ .<sup>69</sup> It seemed that  $^1\text{O}_2$  played an important role because  $k_{app}$  dropped by 34.0% in the presence of FFA (Fig. 4b and S6c†). To verify the contribution of  $^1\text{O}_2$ , the  $\text{H}_2\text{O}$  solvent was replaced by  $\text{D}_2\text{O}$ . Since  $^1\text{O}_2$  possessed a much longer lifetime in  $\text{D}_2\text{O}$  ( $55 \mu\text{s}$ ) than that in  $\text{H}_2\text{O}$  ( $4 \mu\text{s}$ ),<sup>70</sup> the removal of CBB should be accelerated if  $^1\text{O}_2$  played an essential role. However,  $k_{app}$  remained almost unchanged after solvent exchange (Fig. 4b), and the suppression effect brought by FFA was attributed to its direct reaction with PMS rather than the quenching of  $^1\text{O}_2$ .<sup>71</sup> In summary,  $\cdot\text{OH}$ ,  $\text{SO}_4^{\cdot-}$  and high-valent iron species were the dominant species for the degradation of CBB in the MGO/PMS system, while the contributions of  $\text{O}_2^{\cdot-}$  and  $^1\text{O}_2$  were limited.

When carbonaceous materials were used as catalysts for PMS activation, the non-radical electron-transfer pathway was usually involved.<sup>72,73</sup> The *in situ* OCP test is a useful tool to characterize the electron-transfer pathway, where the potential of catalyst increased with PMS addition and then decreased with the addition of organic pollutants, indicating that





metastable catalyst-PMS\* complex was formed and then oxidized the pollutants.<sup>72,73</sup> However, in the current work, although the potential of MGO was raised upon the addition of PMS, the subsequent addition of CBB did not trigger a decrease but an increase in its potential (Fig. S6d†). Thus, it was inferred that the metastable catalyst-PMS\* was formed but did not participate in the oxidation of CBB. Considering the abundant functionalities on GO surface, its conductivity should be much lower than the carbonaceous materials such as CNT and highly graphitized carbons in previous works,<sup>72,73</sup> hindering the non-radical electron-transfer pathway. The result here is also different from previous works where the non-radical electron-transfer pathway was found to play an indispensable role using Fe<sub>3</sub>O<sub>4</sub>/graphene<sup>24</sup> and Fe<sub>3</sub>O<sub>4</sub>/rGO<sup>25</sup> as catalysts. This is also ascribed to the higher oxygen content and thus lower conductivity of GO compared to graphene and rGO.

Looking back to the 87.1% CBB removal obtained in the MGO/PMS/MA + PMSO system, it could be safely concluded that this relatively high removal was ascribed to the contribution of adsorption as well as direct oxidative reaction between CBB and PMS. Similar to the case discussed in Section 3.3, the contribution of direct oxidation could not be simply calculated by subtracting the removal value in the MGO/PMS/MA + PMSO system (87.1%) from the value obtained by adsorption at pH 2.7 (84.2%). This is also reflected from the results of extraction tests. As shown in Fig. S3,† the colors of the extracted sample obtained in the MGO/PMS/MA + PMSO system (Fig. S3c†) were considerable lighter than those obtained after adsorption only (Fig. S3b†). That is to say, although the removals in the aqueous phase were similar for MGO and MGO/PMS/MA + PMSO systems, the concentration of CBB in the solid phase was much lower in the latter case due to direct oxidation of CBB by PMS. Similarly, compared to the samples obtained in the MGO/PMS system (Fig. S3a†), the concentration of CBB in the solid phase in the MGO/PMS/MA + PMSO system was considerably higher. When both MA and PMSO were added, the catalytic oxidation process was significantly suppressed not only in the aqueous phase but also in the solid phase. Under this condition, the suppression effect of MA and PMSO was underestimated by observing the change in aqueous CBB removal.

### 3.7. Degradation pathway and toxicity evaluation

As mentioned in Section 3.2, the lower TOC removal compared to CBB removal indicated the formation of organic products in the catalytic oxidation process. This is also reflected from the higher absorbances at 200–400 nm in the spectrum of CBB after oxidation (Fig. S2a†). Thus, the aqueous sample after treatment with the MGO/PMS system was analyzed by LC-MS to identify the oxidation products. Considering the large molecular weight and complex structure of CBB, the orbital-weighted Fukui functions of CBB were calculated to assist the analysis of its degradation pathway. The orbital-weighted Fukui functions of  $f_{ow}^-$  and  $f_{ow}^0$  were depicted in Fig. 5, which represented the tendency of electrophilic attack and radical attack respectively.<sup>74,75</sup> It could be observed that the most positive part of  $f_{ow}^-$  was localized on N34, N63 and N88, indicating that these

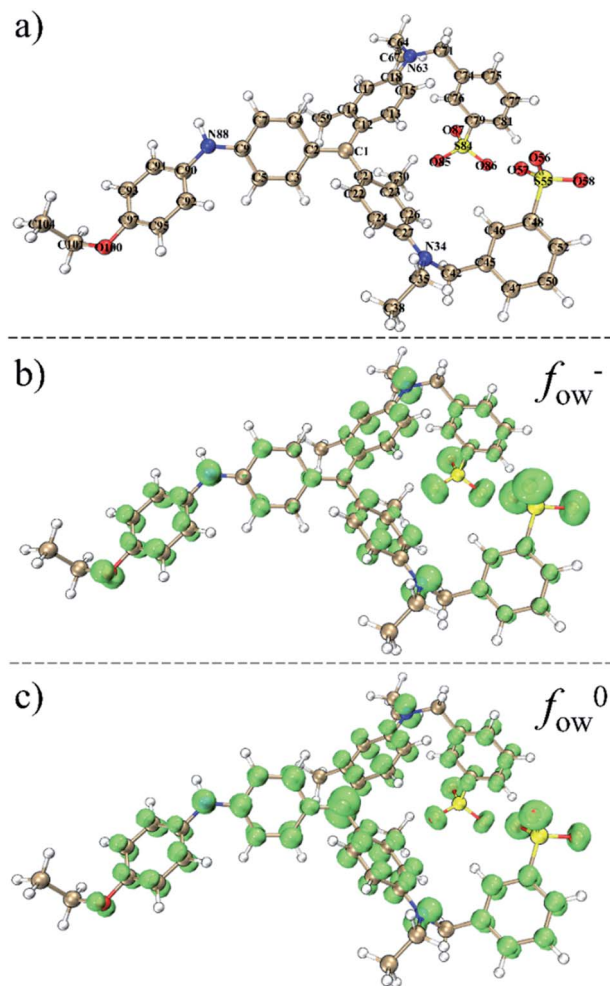


Fig. 5 The optimized molecular structure of CBB (a) and the orbital-weighted Fukui functions of  $f_{ow}^-$  (b) and  $f_{ow}^0$  (c). The green isosurface corresponds positive regions of  $f_{ow}^-$  and  $f_{ow}^0$ .

sites were more favorable for electrophilic attack. Here the oxygen sites were not considered because the large values around them were mainly attributed to the electronegativity of oxygen and electrophilic attack could unlikely occur there.<sup>76</sup> For  $f_{ow}^0$ , the most positive part was localized on C1, suggesting the strong tendency of radical attack on this site. In addition, the condensed Fukui indexes for  $f_{ow}^-$  and  $f_{ow}^0$  were calculated and listed in Table S3.† The highest  $f_{ow}^-$  values for N34 (0.2748), N63 (0.2845) and N88 (0.2233) as well as the highest  $f_{ow}^0$  value for C1 (0.4283) also suggested that these sites were vulnerable in the oxidation process of CBB.

Based on MS results (Fig. S7†), the above analysis and the previous report,<sup>33</sup> the plausible degradation pathway of CBB was proposed and illustrated in Fig. 6. The attack on the N34 or N63 site of **A** (parent CBB) resulted in formation of **B** and release of **C**. Meanwhile, the attack on the N88 site of **A** led to the formation of **D** and **E**. Furthermore, the attack on the C1 site of **B** resulted in the formation of **H** and **I**, which underwent further attack on the nitrogen sites to form **N** and **O**. The attack on the C1 site of **D** led to the formation of **K**, which transformed into **P**



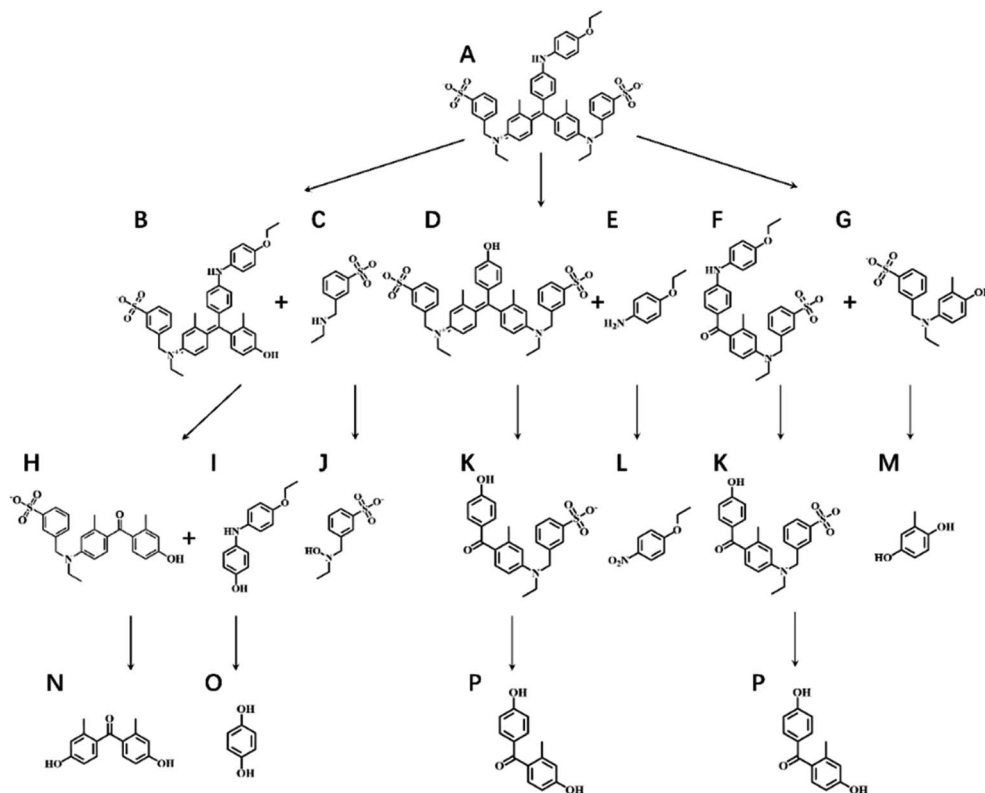


Fig. 6 The plausible degradation pathway of CBB.

subsequently through attack on its nitrogen site. For the attack on the C1 site of A, oxidation products of F and G are expected, and further attack on the nitrogen sites of them resulted in the formation of K and M. The secondary amine group in the released smaller product of C was further oxidized to hydroxyl amine, leading to the formation of J. The released smaller

product of E possessed a primary amine group, which was further oxidized to L with a nitro group.

Since a variety of degradation products were formed, the toxicity variation in the degradation process should be evaluated. Thus, the ecotoxicity of CBB and its degradation products was estimated by the ECOSAR program using aquatic species of

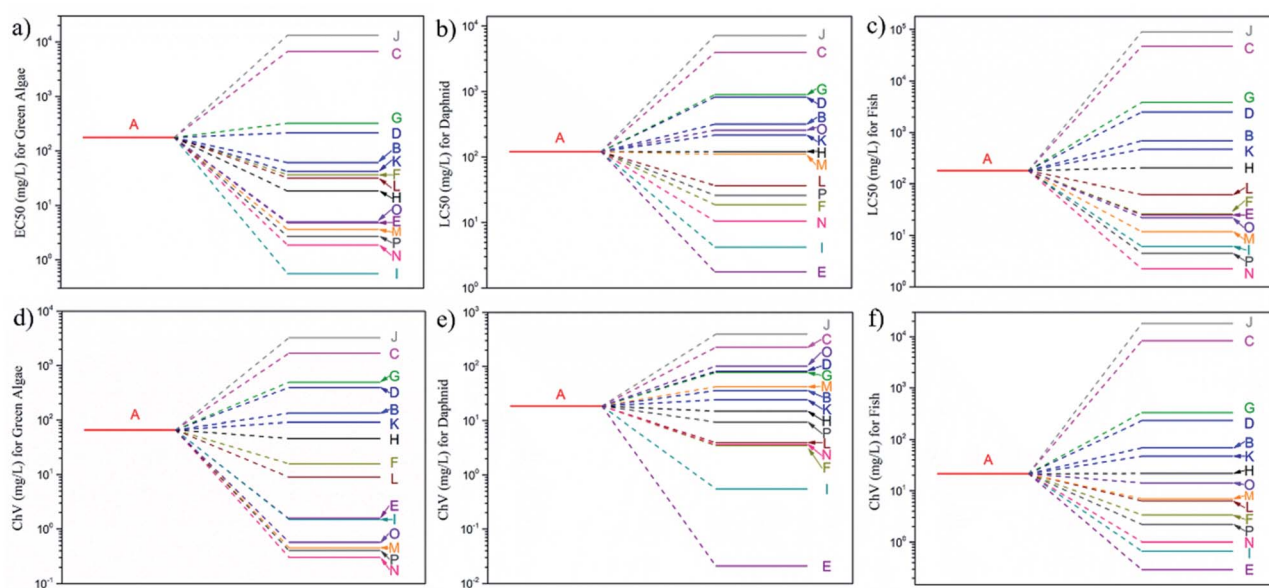


Fig. 7 Acute (a–c) and chronic toxicity (d–f) of CBB and its degradation products for green algae, daphnia, and fish.

three trophic levels (green algae, daphnia, and fish) as indicators. As shown in Fig. 7, CBB and its degradation products showed different toxicity for the three indicator species. The products **J**, **C**, **G** and **D** possessed higher EC50/LC50 values than **A** (the parent CBB) for all the three species (Fig. 7a–c), indicating decreased acute toxicity of them. From the aspect of chronic toxicity (Fig. 7d–f), besides the above four products, other two products **B** and **K** were also less toxic compared to **A**. For the product **O**, the higher LC50 and ChV values compared to those of **A** for daphnid suggested its declined toxicity. However, lower EC50/LC50 and ChV values for green algae and fish were also observed, suggesting increased toxicity for these two species. This divergency indicated the trophic-level dependent toxicity of some products. Besides, products with increased toxicity were also observed. According to the Globally Harmonized System of Classification and Labelling of Chemicals, chemicals with EC50/LC50/ChV values lower than 1 mg L<sup>-1</sup> are considered as very toxic.<sup>77,78</sup> As shown in Fig. 7a, the product **I** with an EC50 for green algae less than 1 mg L<sup>-1</sup> should be classified as very toxic. From the chronic toxicity aspect (Fig. 7d–f), more products including **O**, **M**, **P**, **N** and **E** should be considered as very toxic, which should rouse attention for potential practical applications. In this sense, further research on the following aspects may to be conducted. On the one hand, considering the different concentrations of the products and their potential joint toxicity effects, toxicity experiments may help to reveal the overall toxicity of the treated water. On the other hand, when optimizing the operation conditions, changing the target to achieving lower toxicities may help to reduce potential environmental risks. In addition, after catalytic oxidation, the resulting water may be further treated by adsorption, membrane filtration or other technologies for the removal of those remaining toxic oxidation products.

## 4. Conclusions

The Fe<sub>3</sub>O<sub>4</sub>-GO composite material was prepared and used as a catalyst to activate PMS for degradation of CBB. The effects of several operation conditions including MGO dosage, PMS dosage and initial concentration of CBB were studied. CBB removal could reach 99.5% at 0.5 g L<sup>-1</sup> MGO and 2 mM PMS when the initial CBB concentration was 50 mg L<sup>-1</sup>, and the removal of TOC under this condition was found to be 50.9%. High removals of 98.4–99.9% were also achieved for other dyes with varied structures including MO, MB, RhB and BB17, verifying the wide applicability of the MGO/PMS catalytic system. The effects of environmental factors were also investigated. High CBB removals could be achieved in a wide initial pH range of 2.7–11.0 and in the presence of inorganic ions including Cl<sup>-</sup>, HCO<sub>3</sub><sup>-</sup> and HPO<sub>4</sub><sup>2-</sup>. The removal efficiencies in tap water and lake water were slightly lower than that in DI water, and the accelerated removal in sea water was ascribed to the high concentration of Cl<sup>-</sup> ions. Reusability test showed that CBB removals maintained above 90% in five consecutive runs, indicating the acceptable recyclability of MGO. Based on quenching experiments, solvent exchange (H<sub>2</sub>O to D<sub>2</sub>O) and *in situ* OCP test, it was concluded that <sup>•</sup>OH, SO<sub>4</sub><sup>•-</sup> and high-valent

iron species were responsible for the efficient degradation of CBB in the MGO/PMS system, while the contributions of O<sub>2</sub><sup>•-</sup>, <sup>1</sup>O<sub>2</sub> and the non-radical electron-transfer pathway were limited. Furthermore, based on DFT calculations and LC-MS results, the plausible degradation pathway of CBB was proposed. Finally, toxicity variation in the degradation process was evaluated by SARs using green algae, daphnia, and fish as indicator species, and the trophic-level dependent toxicity of the degradation products was observed. Although some products possessed decreased acute and chronic toxicity compared to the parent CBB, the presence of some very toxic products should rouse attention for potential practical applications. Further research on toxicity experiments, process optimization for lower toxicities as well as combination with other treatment technologies should be conducted.

## Abbreviation list

AOP	Advanced oxidation process
BB17	Basic blue 17
BQ	Benzoquinone
CBB	Coomassie brilliant blue G250
DFT	Density functional theory
DI	Deionized
ECOSAR	Ecological structure–activity relationships
ESI	Electron spray ionization
FFA	Furfuryl alcohol
FMO	Frontier molecular orbital
FTIR	Fourier transform infrared
GO	Graphene oxide
ICP-MS	Inductively coupled plasma-mass spectrometry
IEP	Isoelectric point
LC-MS	Liquid chromatography-mass spectrometry
MA	Methanol
MB	Methylene blue
MGO	Magnetic graphene oxide
MO	Methyl orange
OCP	Open circuit potential
PDS	Peroxydisulfate
PMS	Peroxymonosulfate
PMSO	Methyl phenyl sulfoxide
rGO	Reduced graphene oxide
RhB	Rhodamine B
ROSs	Reactive oxygen species
SARs	Structure–activity relationships
SMS	Solvation model based on density
TBA	<i>Tert</i> -butanol
TEM	Transmission electron microscopy
TOC	Total organic carbon
UPLC	Ultra-high performance liquid chromatography
VMD	Virtual molecular dynamic
VSM	Vibrating sample magnetometry
XPS	X-ray photoelectron spectroscopy
XRD	X-ray diffraction



## Author contributions

Yawei Shi: writing – original draft, writing – review & editing, conceptualization. Haonan Wang: methodology, data curation, investigation. Guobin Song: formal analysis, data curation. Yi Zhang: investigation. Liya Tong: investigation. Ya Sun: resources. Guanghui Ding: resources, supervision.

## Conflicts of interest

The authors declare that they have no known competing financial interests or personal relationships that could have appeared to influence the work reported in this paper.

## Acknowledgements

This work is financially supported by the Joint Research Fund Liaoning-Shenyang National Laboratory for Materials Science (20180510004) and the National Natural Science Foundation of China (51479016, 51908409).

## References

- 1 X. Zheng, X. Niu, D. Zhang, M. Lv, X. Ye, J. Ma, Z. Lin and M. Fu, Metal-based catalysts for persulfate and peroxymonosulfate activation in heterogeneous ways: A review, *Chem. Eng. J.*, 2022, **429**, 132323.
- 2 X. Duan, H. Sun and S. Wang, Metal-free carbocatalysis in advanced oxidation reactions, *Acc. Chem. Res.*, 2018, **51**, 678–687.
- 3 R. R. Solis, I. F. Mena, M. N. Nadagouda and D. D. Dionysiou, Adsorptive interaction of peroxymonosulfate with graphene and catalytic assessment via non-radical pathway for the removal of aqueous pharmaceuticals, *J. Hazard. Mater.*, 2020, **384**, 121340.
- 4 Y. Ji, J. Lu, L. Wang, M. Jiang, Y. Yang, P. Yang, L. Zhou, C. Ferronato and J.-M. Chovelon, Non-activated peroxymonosulfate oxidation of sulfonamide antibiotics in water: Kinetics, mechanisms, and implications for water treatment, *Water Res.*, 2018, **147**, 82–90.
- 5 B. Yang, Q. Luo, Q. Li, Y. Meng, L. Lingli and Y. Liu, Selective oxidation and direct decolorization of cationic dyes by persulfate without activation, *Water Sci. Technol.*, 2021, **83**, 2744–2752.
- 6 X. Pan, L. Yan, R. Qu and Z. Wang, Degradation of the UV-filter benzophenone-3 in aqueous solution using persulfate activated by heat, metal ions and light, *Chemosphere*, 2018, **196**, 95–104.
- 7 D. Tian, H. Zhou, H. Zhang, P. Zhou, J. You, Y. Gang, Z. Pan, Y. Liu and B. Lai, Heterogeneous photocatalyst-driven persulfate activation process under visible light irradiation: From basic catalyst design principles to novel enhancement strategies, *Chem. Eng. J.*, 2022, **428**, 131166.
- 8 G. Z. Kyzas, N. Mengelizadeh, M. k. Saloot, S. Mohebi and D. Balarak, Sonochemical degradation of ciprofloxacin by hydrogen peroxide and persulfate activated by ultrasound and ferrous ions, *Colloids Surf., A*, 2022, **642**, 128627.
- 9 X. Chen, N. Zhao and X. Hu, A novel strategy of pulsed electro-assisted pyrite activation of peroxymonosulfate for the degradation of tetracycline hydrochloride, *Sep. Purif. Technol.*, 2022, **280**, 119781.
- 10 G. Zhao, J. Zou, X. Chen, L. Liu, Y. Wang, S. Zhou, X. Long, J. Yu and F. Jiao, Iron-based catalysts for persulfate-based advanced oxidation process: Microstructure, property and tailoring, *Chem. Eng. J.*, 2021, **421**, 127845.
- 11 R. Keyikoglu, O. Karatas, A. Khataee, M. Kobya, O. T. Can, R. Darvishi Cheshmeh Soltani and M. Isleyen, Peroxydisulfate activation by in situ synthesized Fe<sub>3</sub>O<sub>4</sub> nanoparticles for degradation of atrazine: Performance and mechanism, *Sep. Purif. Technol.*, 2020, **247**, 116925.
- 12 J. Lu, Y. Zhou, J. Lei, Z. Ao and Y. Zhou, Fe<sub>3</sub>O<sub>4</sub>/graphene aerogels: A stable and efficient persulfate activator for the rapid degradation of malachite green, *Chemosphere*, 2020, **251**, 126402.
- 13 D. Li, T. Hua, J. Yuan and F. Xu, Methylene blue adsorption from an aqueous solution by a magnetic graphene oxide/humic acid composite, *Colloids Surf., A*, 2021, **627**, 127171.
- 14 H. Guo, Z. Li, S. Lin, D. Li, N. Jiang, H. Wang, J. Han and J. Li, Multi-catalysis induced by pulsed discharge plasma coupled with graphene-Fe<sub>3</sub>O<sub>4</sub> nanocomposites for efficient removal of ofloxacin in water: Mechanism, degradation pathway and potential toxicity, *Chemosphere*, 2021, **265**, 129089.
- 15 L. Li, C. Liu, R. Ma, Y. Yu, Z. Chang, X. Zhang, C. Yang, D. Chen, Y. Yu, W. Li and Y. Liu, Enhanced oxidative and adsorptive removal of thallium(I) using Fe<sub>3</sub>O<sub>4</sub>@TiO<sub>2</sub> decorated RGO nanosheets as persulfate activator and adsorbent, *Sep. Purif. Technol.*, 2021, **271**, 118827.
- 16 G. Ersan, O. G. Apul, F. Perreault and T. Karanfil, Adsorption of organic contaminants by graphene nanosheets: A review, *Water Res.*, 2017, **126**, 385–398.
- 17 H. Sun, S. Liu, G. Zhou, H. M. Ang, M. O. Tade and S. Wang, Reduced graphene oxide for catalytic oxidation of aqueous organic pollutants, *ACS Appl. Mater. Interfaces*, 2012, **4**, 5466–5471.
- 18 H. Chen and K. C. Carroll, Metal-free catalysis of persulfate activation and organic-pollutant degradation by nitrogen-doped graphene and aminated graphene, *Environ. Pollut.*, 2016, **215**, 96–102.
- 19 S. Wang, L. Xu and J. Wang, Nitrogen-doped graphene as peroxymonosulfate activator and electron transfer mediator for the enhanced degradation of sulfamethoxazole, *Chem. Eng. J.*, 2019, **375**, 122041.
- 20 T. Olmez-Hanci, I. Arslan-Alaton, S. Gurmen, I. Gafarli, S. Khoei, S. Safaltin and D. Yesiltepe Ozelcik, Oxidative degradation of Bisphenol A by carbocatalytic activation of persulfate and peroxymonosulfate with reduced graphene oxide, *J. Hazard. Mater.*, 2018, **360**, 141–149.
- 21 L. Chen, P. Hu, L. Zhang, S. Huang, L. Luo and C. Huang, Toxicity of graphene oxide and multi-walled carbon nanotubes against human cells and zebrafish, *Sci. China Chem.*, 2012, **55**, 2209–2216.
- 22 Y. Shi, H. Wang, G. Song, Y. Zhang, L. Tong, Y. Sun and G. Ding, Magnetic graphene oxide for methylene blue removal: adsorption performance and comparison of





- regeneration methods, *Environ. Sci. Pollut. Res.*, 2022, **29**(29), 30774–30789.
- 23 X.-B. Gong, Degradation of dye wastewater by persulfate activated with  $\text{Fe}_3\text{O}_4$ /graphene nanocomposite, *J. Water Reuse Desalin.*, 2016, **6**, 553–561.
  - 24 R. R. Solís, Ö. Dinc, G. Fang, M. N. Nadagouda and D. D. Dionysiou, Activation of inorganic peroxides with magnetic graphene for the removal of antibiotics from wastewater, *Environ. Sci.: Nano*, 2021, **8**, 960–977.
  - 25 F. Yin, C. Wang, K.-Y. A. Lin and S. Tong, Persulfate activation for efficient degradation of norfloxacin by a rGO- $\text{Fe}_3\text{O}_4$  composite, *J. Taiwan Inst. Chem. Eng.*, 2019, **102**, 163–169.
  - 26 W. Wang, Y. Cao, X. Hu, S. Zhou, D. Zhu, D. Qi and S. Deng, Granular reduced graphene oxide/ $\text{Fe}_3\text{O}_4$  hydrogel for efficient adsorption and catalytic oxidation of p-perfluorous nonenoxbenzene sulfonate, *J. Hazard. Mater.*, 2020, **386**, 121662.
  - 27 X. Meng, Q. He, T. Song, M. Ge, Z. He and C. Guo, Activation of peroxydisulfate by magnetically separable rGO/ $\text{MnFe}_2\text{O}_4$  toward oxidation of tetracycline: Efficiency, mechanism and degradation pathways, *Sep. Purif. Technol.*, 2022, **282**, 120137.
  - 28 N. H. Adenan, Y. Y. Lim and A. S. Y. Ting, Removal of triphenylmethane dyes by *Streptomyces bacillaris*: A study on decolorization, enzymatic reactions and toxicity of treated dye solutions, *J. Environ. Manage.*, 2022, **318**, 115520.
  - 29 E. Brunelle, A. M. Le, C. Huynh, K. Wingfield, L. Halámková, J. Agudelo and J. Halánek, Coomassie Brilliant Blue G-250 dye: an application for forensic fingerprint analysis, *Anal. Chem.*, 2017, **89**, 4314–4319.
  - 30 J. Zhao, Q.-X. Wu, X.-D. Cheng, T. Su, X.-H. Wang, W.-N. Zhang, Y.-M. Lu and Y. Chen, Biodegradation and detoxification of the triphenylmethane dye coomassie brilliant blue by the extracellular enzymes from mycelia of *Lactarius deliciosus*, *Front. Chem. Sci. Eng.*, 2020, **15**, 421–436.
  - 31 M. A. Rauf, S. Ashraf and S. N. Alhadrami, Photolytic oxidation of Coomassie Brilliant Blue with  $\text{H}_2\text{O}_2$ , *Dye Pigm.*, 2005, **66**, 197–200.
  - 32 S. B. Bukallah, M. A. Rauf and S. S. Ashraf, Photocatalytic decoloration of Coomassie Brilliant Blue with titanium oxide, *Dyes Pigm.*, 2007, **72**, 353–356.
  - 33 M. P. Rayaroth, U. K. Aravind and C. T. Aravindakumar, Sonochemical degradation of Coomassie Brilliant Blue: effect of frequency, power density, pH and various additives, *Chemosphere*, 2015, **119**, 848–855.
  - 34 S. Baradaran and M. T. Sadeghi, Coomassie Brilliant Blue (CBB) degradation using hydrodynamic cavitation, hydrogen peroxide and activated persulfate ( $\text{HC-H}_2\text{O}_2$ -KPS) combined process, *Chem. Eng. Process.*, 2019, **145**, 107674.
  - 35 M. C. Collivignarelli, A. Abba, M. Carnevale Miino and S. Damiani, Treatments for color removal from wastewater: State of the art, *J. Environ. Manage.*, 2019, **236**, 727–745.
  - 36 H. Chi, J. Wan, X. Zhou, J. Sun and B. Yan,  $\text{Fe}@C$  activated peroxymonosulfate system for effectively degrading emerging contaminants: Analysis of the formation and activation mechanism of Fe coordinately unsaturated metal sites, *J. Hazard. Mater.*, 2021, **419**, 126535.
  - 37 M. J. Frisch, G. W. Trucks, H. B. Schlegel, G. E. Scuseria, M. A. Robb and J. R. Cheeseman, et. al., *Gaussian 16 Rev. C.01*, Gaussian, Inc., Wallingford CT, 2016.
  - 38 T. Lu and F. Chen, Multiwfn: a multifunctional wavefunction analyzer, *J. Comput. Chem.*, 2012, **33**, 580–592.
  - 39 W. Humphrey, A. Dalke and K. Schulten, VMD: visual molecular dynamics, *J. Mol. Graphics*, 1996, **14**, 33–38.
  - 40 R. Pino-Rios, O. Yañez, D. Inostroza, L. Ruiz, C. Cardenas, P. Fuentealba and W. Tiznado, Proposal of a simple and effective local reactivity descriptor through a topological analysis of an orbital-weighted fukui function, *J. Comput. Chem.*, 2017, **38**, 481–488.
  - 41 R. Pino-Rios, D. Inostroza, G. Cárdenas-Jirón and W. Tiznado, Orbital-weighted dual descriptor for the study of local reactivity of systems with (quasi-) degenerate states, *J. Phys. Chem. A*, 2019, **123**, 10556–10562.
  - 42 Y. Shi, J. Zhu, G. Yuan, G. Liu, Q. Wang, W. Sun, B. Zhao, L. Wang and H. Zhang, Activation of persulfate by EDTA-2K-derived nitrogen-doped porous carbons for organic contaminant removal: Radical and non-radical pathways, *Chem. Eng. J.*, 2020, **386**, 124009.
  - 43 X. Pan, C. Li, J. Chen, J. Liu, J. Ge, J. Yao, S. Wang, Z. Wang, R. Qu and A. Li, The photodegradation of 1,3,6,8-tetrabromocarbazole in n-hexane and in solid-mediated aqueous system: Kinetics and transformation mechanisms, *Chem. Eng. J.*, 2019, **375**, 121986.
  - 44 Y. Pang, J. Zhou, X. Yang, Y. Lan and C. Chen, Rationally designed  $\text{Co}_3\text{O}_4\text{-SnO}_2$  activated peroxymonosulfate for the elimination of chloramphenicol, *Chem. Eng. J.*, 2021, **418**, 129401.
  - 45 B.-T. Zhang, W. Xiang, X. Jiang, Y. Zhang and Y. Teng, Oxidation of Dyes by Alkaline-Activated Peroxymonosulfate, *J. Environ. Eng.*, 2016, **142**, 04016003.
  - 46 C. Qi, X. Liu, J. Ma, C. Lin, X. Li and H. Zhang, Activation of peroxymonosulfate by base: Implications for the degradation of organic pollutants, *Chemosphere*, 2016, **151**, 280–288.
  - 47 Z. Wu, Y. Wang, Z. Xiong, Z. Ao, S. Pu, G. Yao and B. Lai, Core-shell magnetic  $\text{Fe}_3\text{O}_4@Zn/Co$ -ZIFs to activate peroxymonosulfate for highly efficient degradation of carbamazepine, *Appl. Catal., B*, 2020, **277**, 119136.
  - 48 C. Yin, Q. Xia, J. Zhou, B. Li, Y. Guo, A. Khan, X. Li and A. Xu, Direct electron transfer process-based peroxymonosulfate activation via surface labile oxygen over mullite oxide  $\text{YMn}_2\text{O}_5$  for effective removal of bisphenol A, *Sep. Purif. Technol.*, 2022, **280**, 119924.
  - 49 Q. Wang, Y. Shao, N. Gao, W. Chu, J. Chen, X. Lu, Y. Zhu and N. An, Activation of peroxymonosulfate by  $\text{Al}_2\text{O}_3$ -based  $\text{CoFe}_2\text{O}_4$  for the degradation of sulfachloropyridazine sodium: Kinetics and mechanism, *Sep. Purif. Technol.*, 2017, **189**, 176–185.
  - 50 N. An, M. Zhao, X. Zheng, Q. Wang, X. Huang, B. Sun, Y. Shen, J. Wang, B. Chen and R. Liu, Synergistic oxytetracycline adsorption and peroxydisulfate-driven



- oxidation on nitrogen and sulfur co-doped porous carbon spheres, *J. Hazard. Mater.*, 2022, **424**, 127444.
- 51 L. Liang, X. Yue, S. Dong, J. Feng, J. Sun, Y. Pan and M. Zhou, New insights into the effect of adsorption on catalysis in the metal-free persulfate activation process for removing organic pollutants, *Sep. Purif. Technol.*, 2021, **272**, 118923.
  - 52 C. Luo, D. Wu, L. Gan, X. Cheng, Q. Ma, F. Tan, J. Gao, W. Zhou, S. Wang, F. Zhang and J. Ma, Oxidation of Congo red by thermally activated persulfate process: Kinetics and transformation pathway, *Sep. Purif. Technol.*, 2020, **244**, 116839.
  - 53 J. Peng, Z. Wang, S. Wang, J. Liu, Y. Zhang, B. Wang, Z. Gong, M. Wang, H. Dong, J. Shi, H. Liu, G. Yan, G. Liu, S. Gao and Z. Cao, Enhanced removal of methylparaben mediated by cobalt/carbon nanotubes (Co/CNTs) activated peroxymonosulfate in chloride-containing water: Reaction kinetics, mechanisms and pathways, *Chem. Eng. J.*, 2021, **409**, 128176.
  - 54 F. Wang, H. Fu, F.-X. Wang, X.-W. Zhang, P. Wang, C. Zhao and C.-C. Wang, Enhanced catalytic sulfamethoxazole degradation via peroxymonosulfate activation over amorphous  $\text{CoS}_x/\text{SiO}_2$  nanocages derived from ZIF-67, *J. Hazard. Mater.*, 2022, **423**, 116998.
  - 55 J.-C. E. Yang, M.-P. Zhu, D. D. Dionysiou, B. Yuan and M.-L. Fu, Interplay of bicarbonate and the oxygen-containing groups of carbon nanotubes dominated the metal-free activation of peroxymonosulfate, *Chem. Eng. J.*, 2022, **430**, 133102.
  - 56 P. Duan, X. Liu, B. Liu, M. Akram, Y. Li, J. Pan, Q. Yue, B. Gao and X. Xu, Effect of phosphate on peroxymonosulfate activation: Accelerating generation of sulfate radical and underlying mechanism, *Appl. Catal., B*, 2021, **298**, 120532.
  - 57 H. Fu, P. Zhao, S. Xu, G. Cheng, Z. Li, Y. Li, K. Li and S. Ma, Fabrication of  $\text{Fe}_3\text{O}_4$  and graphitized porous biochar composites for activating peroxymonosulfate to degrade p-hydroxybenzoic acid: Insights on the mechanism, *Chem. Eng. J.*, 2019, **375**, 121980.
  - 58 G.-X. Huang, C.-Y. Wang, C.-W. Yang, P.-C. Guo and H.-Q. Yu, Degradation of bisphenol A by peroxymonosulfate catalytically activated with  $\text{Mn}_{1.8}\text{Fe}_{1.2}\text{O}_4$  nanospheres: Synergism between Mn and Fe, *Environ. Sci. Technol.*, 2017, **51**, 12611–12618.
  - 59 Q. Fan, X. Cheng, X. Zhu, C. Luo, H. Ren, D. Wu and H. Liang, Secondary wastewater treatment using peroxymonosulfate activated by a carbon nanofiber supported  $\text{Co}_3\text{O}_4$  ( $\text{Co}_3\text{O}_4/\text{CNF}$ ) catalyst combined with ultrafiltration, *Sep. Purif. Technol.*, 2022, **287**, 120579.
  - 60 J. Wang, X. Duan, Q. Dong, F. Meng, X. Tan, S. Liu and S. Wang, Facile synthesis of N-doped 3D graphene aerogel and its excellent performance in catalytic degradation of antibiotic contaminants in water, *Carbon*, 2019, **144**, 781–790.
  - 61 J. Liang, X. Duan, X. Xu, K. Chen, Y. Zhang, L. Zhao, H. Qiu, S. Wang and X. Cao, Persulfate oxidation of sulfamethoxazole by magnetic iron-char composites via nonradical pathways:  $\text{Fe(IV)}$  versus surface-mediated electron transfer, *Environ. Sci. Technol.*, 2021, **55**, 10077–10086.
  - 62 Y. Feng, Y. Li, B. Yang, Z. Yang, Y. Fan, K. Shih, H. Li, D. Wu and L. Zhang, Mechanistic insight into the generation of high-valent iron-oxo species via peroxymonosulfate activation: An experimental and density functional theory study, *Chem. Eng. J.*, 2021, **420**, 130477.
  - 63 F. Ghanbari and M. Moradi, Application of peroxymonosulfate and its activation methods for degradation of environmental organic pollutants: Review, *Chem. Eng. J.*, 2017, **310**, 41–62.
  - 64 H. Milh, D. Cabooter and R. Dewil, Degradation of sulfamethoxazole by ferrous iron activated peroxymonosulfate: elucidation of the degradation mechanism and influence of process parameters, *Chem. Eng. J.*, 2022, **430**, 132878.
  - 65 L. Gan, L. Wang, L. Xu, X. Fang, C. Pei, Y. Wu, H. Lu, S. Han, J. Cui, J. Shi and C. Mei,  $\text{Fe}_3\text{C}$ -porous carbon derived from  $\text{Fe}_2\text{O}_3$  loaded MOF-74(Zn) for the removal of high concentration BPA: the integrations of adsorptive/catalytic synergies and radical/non-radical mechanisms, *J. Hazard. Mater.*, 2021, **413**, 125305.
  - 66 R. Zhou, S. Lu, Y. Su, T. Li, T. Ma and H. Ren, Hierarchically fusiform  $\text{CuO}$  microstructures decorated with  $\text{Fe}_3\text{O}_4$  nanoparticles as novel persulfate activators for 4-aminobenzenesulfonic acid degradation in aqueous solutions, *J. Alloys Compd.*, 2020, **815**, 152394.
  - 67 X. Li, S. Wang, B. Xu, X. Zhang, Y. Xu, P. Yu and Y. Sun, MOF etching-induced Co-doped hollow carbon nitride catalyst for efficient removal of antibiotic contaminants by enhanced peroxymonosulfate activation, *Chem. Eng. J.*, 2022, **441**, 136074.
  - 68 S. Yang, S. Xu, J. Tong, D. Ding, G. Wang, R. Chen, P. Jin and X. C. Wang, Overlooked role of nitrogen dopant in carbon catalysts for peroxymonosulfate activation: intrinsic defects or extrinsic defects?, *Appl. Catal., B*, 2021, **295**, 120291.
  - 69 Y. Guo, L. Yan, X. Li, T. Yan, W. Song, T. Hou, C. Tong, J. Mu and M. Xu, Goethite/biochar-activated peroxymonosulfate enhances tetracycline degradation: Inherent roles of radical and non-radical processes, *Sci. Total Environ.*, 2021, **783**, 147102.
  - 70 Y.-d. Chen, X. Duan, C. Zhang, S. Wang, N.-q. Ren and S.-H. Ho, Graphitic biochar catalysts from anaerobic digestion sludge for nonradical degradation of micropollutants and disinfection, *Chem. Eng. J.*, 2019, **384**, 123244.
  - 71 W. Ren, L. Xiong, X. Yuan, Z. Yu, H. Zhang, X. Duan and S. Wang, Activation of peroxydisulfate on carbon nanotubes: electron-transfer mechanism, *Environ. Sci. Technol.*, 2019, **53**, 14595–14603.
  - 72 W. Ren, L. Xiong, G. Nie, H. Zhang, X. Duan and S. Wang, Insights into the electron-transfer regime of peroxydisulfate activation on carbon nanotubes: the role of oxygen functional groups, *Environ. Sci. Technol.*, 2020, **54**, 1267–1275.
  - 73 Y. Yu, N. Li, X. Lu, B. Yan, G. Chen, Y. Wang, X. Duan, Z. Cheng and S. Wang, Co/N co-doped carbonized wood



- sponge with 3D porous framework for efficient peroxymonosulfate activation: performance and internal mechanism, *J. Hazard. Mater.*, 2022, **421**, 126735.
- 74 J. Deng, C. Ye, A. Cai, L. Huai, S. Zhou, F. Dong, X. Li and X. Ma, S-doping  $\alpha$ -Fe<sub>2</sub>O<sub>3</sub> induced efficient electron-hole separation for enhanced persulfate activation toward carbamazepine oxidation: Experimental and DFT study, *Chem. Eng. J.*, 2021, **420**, 129863.
- 75 H. Li, Z. Yang, S. Lu, L. Su, C. Wang, J. Huang, J. Zhou, J. Tang and M. Huang, Nano-porous bimetallic CuCo-MOF-74 with coordinatively unsaturated metal sites for peroxymonosulfate activation to eliminate organic pollutants: Performance and mechanism, *Chemosphere*, 2021, **273**, 129643.
- 76 C. Martinez, J. L. Rivera, R. Herrera, J. L. Rico, N. Flores, J. G. Rutiaga and P. Lopez, Evaluation of the chemical reactivity in lignin precursors using the Fukui function, *J. Mol. Model.*, 2008, **14**, 77–81.
- 77 Y. Zhou, J. He, J. Lu, Y. Liu and Y. Zhou, Enhanced removal of bisphenol A by cyclodextrin in photocatalytic systems: Degradation intermediates and toxicity evaluation, *Chinese Chem. Lett.*, 2020, **31**, 2623–2626.
- 78 L. Zhu, Z. Shi and L. Deng, Enhanced heterogeneous degradation of sulfamethoxazole via peroxymonosulfate activation with novel magnetic MnFe<sub>2</sub>O<sub>4</sub>/GCNS nanocomposite, *Colloids Surf., A*, 2021, **621**, 126531.

